Supplementary Information for

The structural basis for activation of voltage sensor domains in an ion channel TPC1

Alexander F. Kintzer†,[1], Evan M. Green†,[1], Pawel K. Dominik†,[1,2], Michael Bridges[3], Jean-Paul Armache[1], Dawid Deneka[2], Sangwoo S. Kim[2], Wayne Hubbell[3], Anthony A. Kossiakoff[2], Yifan Cheng*,[1,4], Robert M. Stroud*,[1]

[1]University of California, San Francisco, Department of Biochemistry and Biophysics

[2]University of Chicago, Department of Biochemistry and Molecular Biology

[3]University of California, Los Angeles, Jules Stein Eye Institute and Department of Chemistry and Biochemistry

[4]Howard Hughes Medical Institute

†These authors contributed equally to this work

Correspondence to Robert Stroud; stroud@msg.ucsf.edu and Yifan Cheng; YCheng@ucsf.edu

This PDF file includes:

Supplementary Discussion
Figs. S1 to S9
Tables S1 to S2
Captions for movies S1
References for SI reference citations

Other supplementary materials for this manuscript include the following:

Movies S1

www.pnas.org/cgi/doi/10.1073/pnas.1805651115

Supplementary Discussion

Structure Determination of AtTPC1$_{DDE}$

Despite the high homogeneity, successful crystallization, and stability of AtTPC1$_{DDE}$ the resolution of crystal diffraction and cryo-EM reconstructions from detergent-purified samples were limited to 7-10Å. We pursued multiple approaches to reconstitute AtTPC1$_{DDE}$ into detergent-free systems for cryo-EM analysis, including amphipols(1), MSP nanodiscs(2), and saposin A nanoparticles (3). Each of the systems produces well-behaved complexes, but only reconstitution into saposin A nanoparticles improved the overall resolution to below 7Å (Fig. S2, S3, See Methods). The relatively low molecular weight of AtTPC1$_{DDE}$ along with the lack of large soluble domains limited the resolution of initial reconstructions. These challenges led us to experiment with various binding reagents as fiducial markers in cryo-EM to facilitate particle alignment at low resolution(4). Llama-derived nanobodies(5) yielded complexes with challenging biochemical properties. The hybridoma(6) approach yielded Fab 4B8 with ~150 nM binding affinity, but the highest resolution obtained did not surpass 7Å. Fab CAT06/H12, one of the 16 antibody fragments generated from synthetic phage display library sorting(7) that bind to AtTPC1 with nanomolar affinities, in conjunction with saposin A nanoparticle reconstitution yielded the best reconstruction ~3.3Å.

AtTPC1$_{DDE}$-CAT06/H12 Interactions

The CDR loops H1-H3 of CAT06/H12 form hydrophobic, hydrogen bonding, and cation-pi interacts with the EF-hand domains and pore 1 of AtTPC1$_{DDE}$ over total interface area of ~740 Å^2 (Fig. S6). CDR H1 (F30, Y33) makes hydrophobic and hydrogen bond contacts with the

EF4 (N384, D386). H2 (Y57, Y58) contacts S12 (Q321) and EF1 (R324). H3 makes extensive van der Waals and hydrogen bond contacts (Y103, W104, W106, R107) with EF1 (R325, F331), the EF1-EF2 loop (K338), and NTD3 (S56). These extensive interactions likely stabilize the EF-hand domains, and the pore, enabling higher resolution reconstructions.

Ion Coordination in the Selectivity Filter

The selectivity filter in $\mathrm{AtTPC1_{WT}}$ and $\mathrm{AtTPC1_{DDE}}$ are equivalent, with a few exceptions described in the main text (Fig. 4). Ion sites 2 and 3 are held in position by backbone (CO) and sidechain (SC) interactions with the S5-S6 and S11-S12 pore loops. Residues S265 (CO 4.1Å, NH 5.8Å), N631 (CO 4.3Å, SC 4.1Å), M629 (CO 5.2Å) coordinate site 2. Residues T263 (CO 5.0Å), T264 (CO 5.8Å, SC 4.2Å), M629 (CO 4.8Å), and V628 (CO 5.8Å) coordinate site 3.

B-factor Analysis of $\mathrm{AtTPC1_{DA}}$

The EF3 and the CTD become disordered in $\mathrm{AtTPC1_{DA}}$ (Fig. 5a). B-factor analysis, a measure of atomic displacement or movement within the crystal, shows that $\mathrm{AtTPC1_{WT}}$ and $\mathrm{AtTPC1_{DA}}$ crystal structures have similar average B-factors ($\mathrm{AtTPC1_{WT}}$ 110 Å^2; $\mathrm{AtTPC1_{DA}}$ 114 Å^2). However, the average B-factors of EF3 in $\mathrm{AtTPC1_{DA}}$ increase from 192 Å^2 to 311 Å^2, precluding accurate placement of most of EF3 including $\mathrm{Ca_a^{2+}}$. Figure 5a was created from refinements of full-length $\mathrm{AtTPC1_{DA}}$ before deleting parts of the CTD and EF-hand domain with high B-factors. Final average B-factors were equivalent between $\mathrm{AtTPC1_{WT}}$ and $\mathrm{AtTPC1_{DA}}$. The CTD, lumenal faces of the VSD1 and 2 containing $\mathrm{Ca_i^{2+}}$, the upper vestibule of the pore, the cytoplasmic face of S9, and the domain 1-2 linker also have markedly increased average B-factors in $\mathrm{AtTPC1_{DA}}$, suggesting that $\mathrm{Ca^{2+}}$-dependent conformational changes in EF3 can influence the conformation of the VSDs, CTD, and the pore domains. Importantly, the observed high B-factor regions in AtTPC1$_{\mathrm{DA}}$ correspond to the regions that undergo conformational change in AtTPC1$_{\mathrm{DDE}}$.

Phosphorylation Sites in the NTD

Phosphorylation can both activate and prevent activation of plant TPC1s (8) and inhibits activation of human TPC1 and 2 (9). Phosphorylation of plant TPC1 by at least two independent kinases can activate or inhibit channel activation. Previously we determined the location of phosphorylation sites in the NTD and CTD of AtTPC1(10, 11). The NTD is clearly resolved in the structure of AtTPC1$_{\mathrm{DDE}}$, enabling complete *de novo* building of residues 20 to 63 (Fig. S4). The NTD contains three helices NTD1 (residues 26-30), NTD2 (residues 33-46), and NTD3 (residues 51-57). We observe density consistent with the three previously identified phosphorylation sites S22, T26, and T29. Phospho-T26 and -T29 both face solvent and could potentially contact the charged phosphatidylcholine headgroups to stabilize the domain. In state 1 and 2 phospho-S22 contacts H410 of the domain 1-2 linker/pre-S7. This contact could influence the conformation of VSD2 depending on the phosphorylation state of S22.

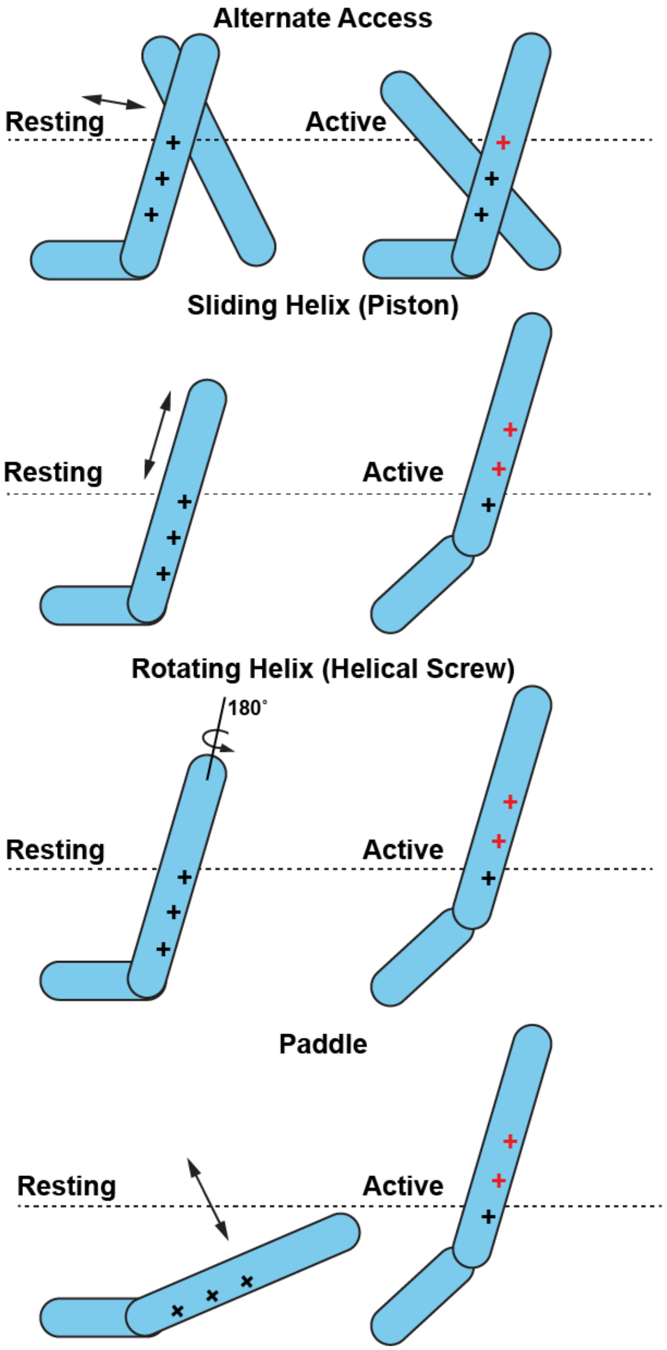

Fig. S1. Mechanisms of VSD activation. Summary of the alternate access mechanism (based on this work), which suggests that S4 does not translate vertically during activation. Rather the VSD helices twist about one another to expose the activated gating charges to solvent on the opposite side of the membrane. Other mechanisms proposed for voltage-dependent activation of VSDs are shown. In the 'Sliding Helix', S4 is proposed to move vertically like a piston. The 'Rotating Helix' or 'Helical Screw' suggests that S4 rotates 180˚ to translate the gating charges (+). The 'Paddle' involves a large rigid-body movement of S4.

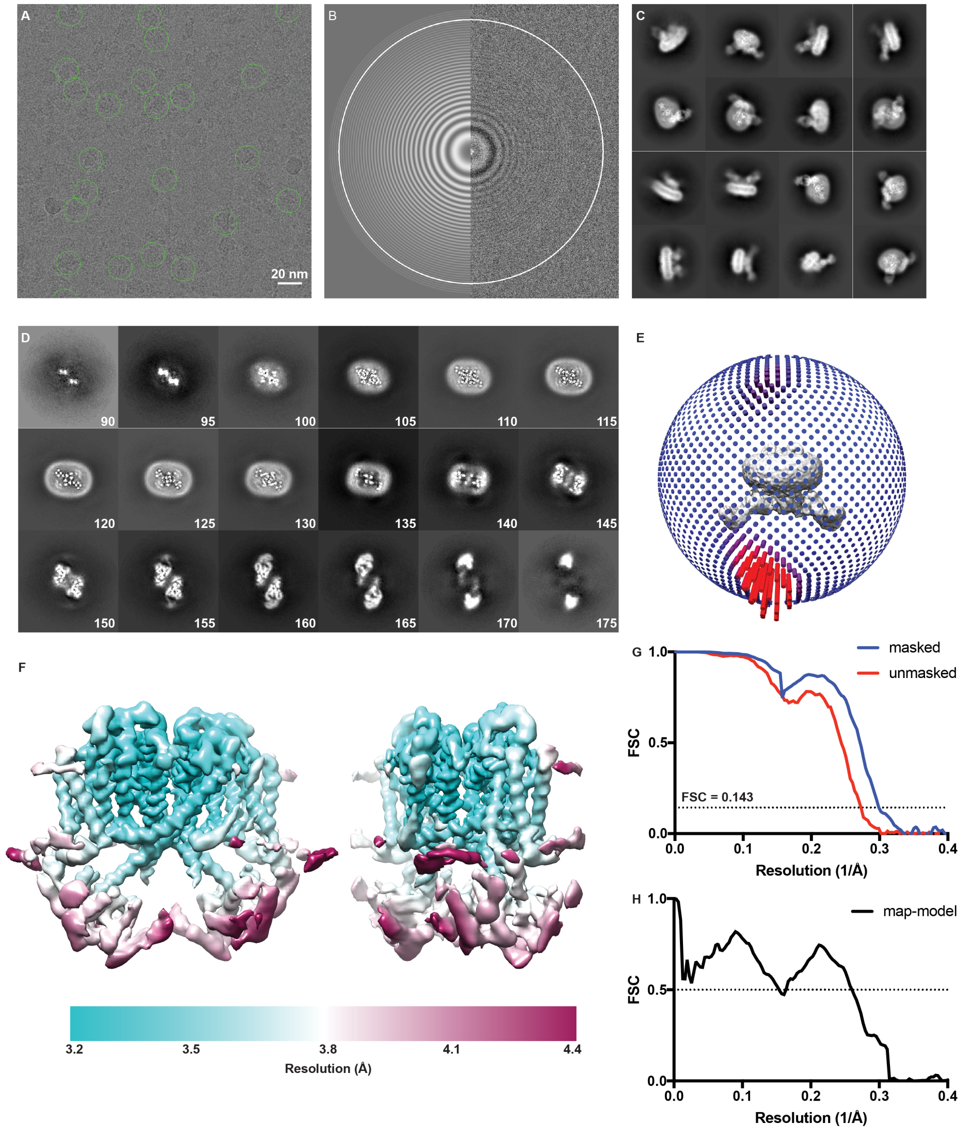

Fig. S2. High-resolution Cryo-EM Structure of AtTPC1$_{\mathbf{DDE}}$. a, Representative motion corrected cryo-EM micrograph of AtTPC1$_{\text{DDE}}$. **b,** Power spectrum of micrograph shown in **(a)** with a 2.8Å estimated CTF resolution as determined by GCTF. **c,** 2D class averages with a particle box size of 128 pixels (311 Å). **d,** Slices through the unsharpened density map at different positions along the channel symmetry axis. Slice numbers starting from the lumenal side are marked. **e,** Euler angle distribution of all particles used for the final 3D reconstruction. The size of each cylinder is proportional to the number of particles with that orientation. **f,** Final unsharpened 3D density map of AtTPC1$_{\text{DDE}}$-Fab-saposin colored with local resolution as estimated by RELION-2. **g,** FSC curves between two independently refined half maps with (blue) and without (red) a mask during post-processing in RELION. **h,** Map-model FSC curve.

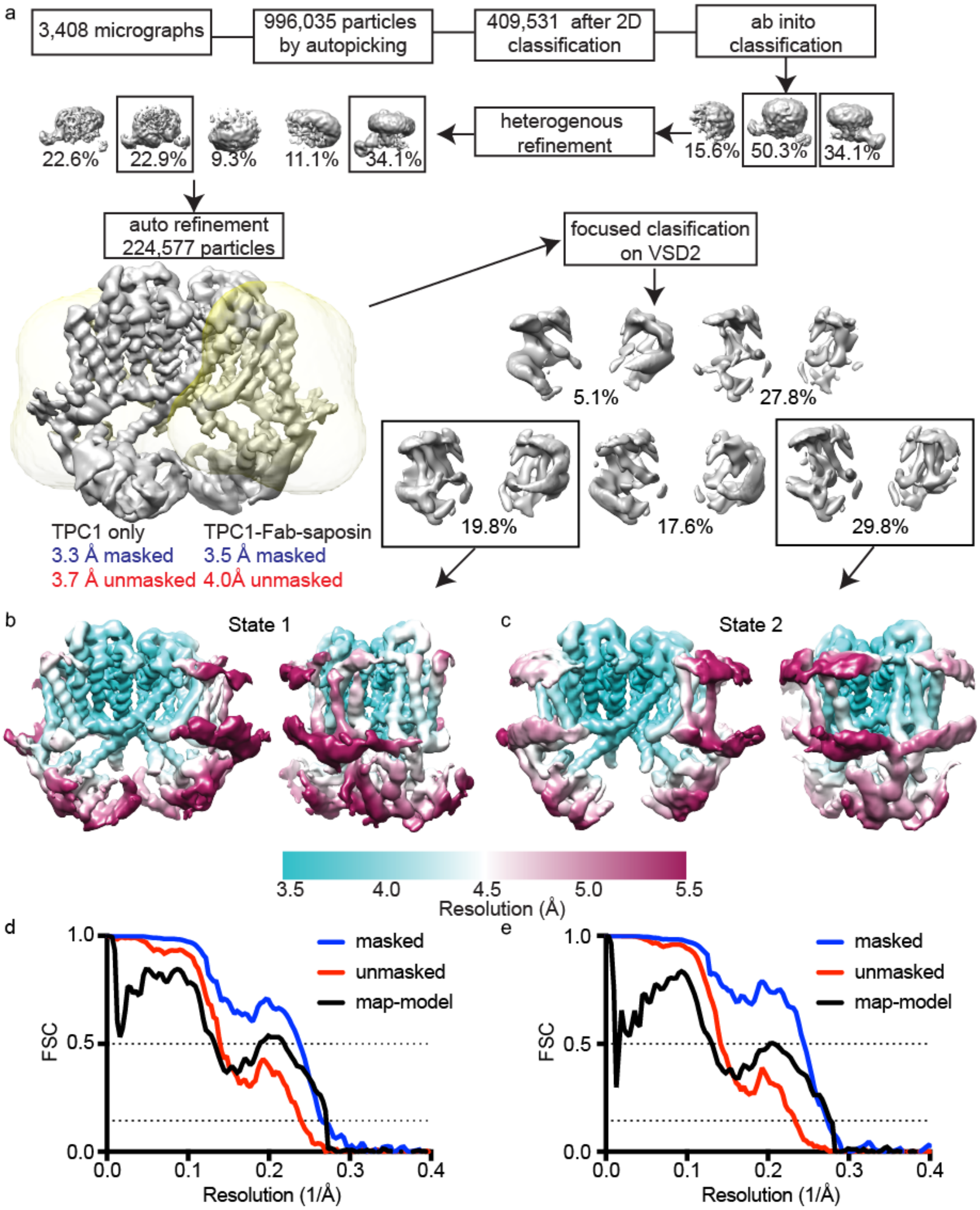

Fig. S3. Cryo-EM Structure Determination of AtTPC1$_{DDE}$ in VSD2 states 1 and 2. a, Image processing pipeline described in Methods. The mask used during focused classification is shown in transparent yellow. Data collection and refinement statistics in Table S1. **b, c,** Final unsharpened 3D density map of AtTPC1$_{DDE}$ colored by local resolution as estimated by RELION-2 for **(b)** state 1 and **(c)** state 2. **d, e,** FSC curves between two independently refined half maps with and without masking and between the map and models for **(d)** state 1 and **(e)** state 2.

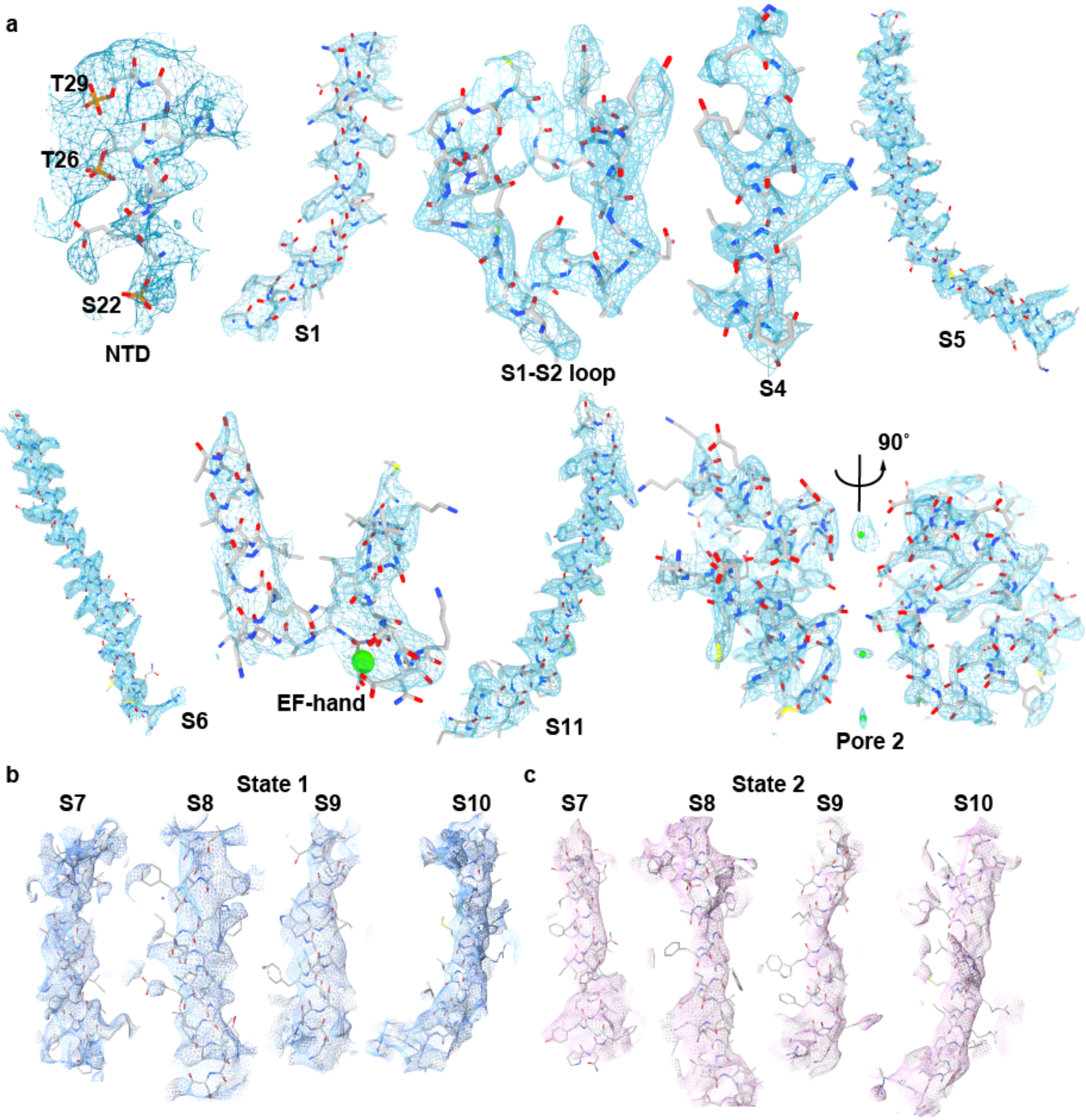

Fig. S4. AtTPC1$_{\mathrm{DDE}}$ cryo-EM density. a, Cryo-EM densities of indicated regions overlaid with atomic model. Density map was sharpened with a B-factor of -117 Å^2. **b, c,** Cryo-EM densities from VSD2 in **(b)** state 1 and **(c)** state 2 overlaid with the atomic model sharpened with B-factors of -95 and -86 Å^2, respectively. Atomic models are colored by atom. Density maps are shown as colored mesh. Ca^{2+}-ions are shown as green spheres.

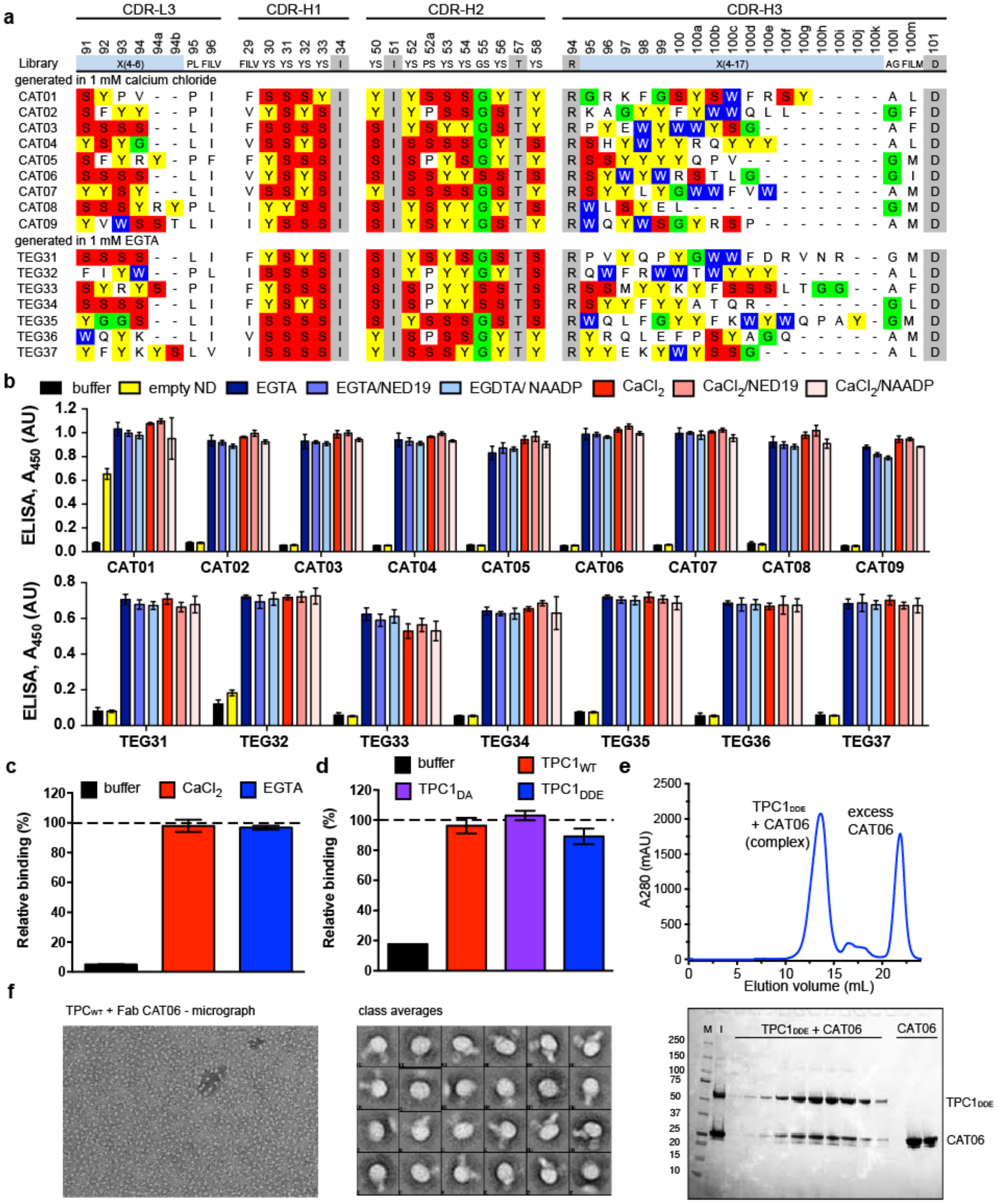

	CDR-L3								CDR-H1						CDR-H2									
	91	92	93	94	94a	94b	95	96	29	30	31	32	33	34	50	51	52	52a	53	54	55	56	57	58
Library	X(4-6)						PL	FILV	FILV	YS	YS	YS	YS	I	YS	I	YS	PS	YS	YS	GS	YS	T	YS
generated in 1 mM calcium chloride																								
CAT01	S	Y	P	V	-	-	P	I	F	S	S	S	Y	I	Y	I	Y	S	S	S	G	Y	T	Y
CAT02	S	F	Y	Y	-	-	P	I	V	Y	S	Y	S	I	Y	I	Y	P	S	S	G	S	T	Y
CAT03	S	S	S	S	-	-	L	I	F	S	S	S	S	I	S	I	Y	S	Y	Y	G	S	T	Y
CAT04	Y	S	Y	G	-	-	L	I	V	S	S	Y	S	I	S	I	S	S	S	S	G	Y	T	S
CAT05	S	F	Y	R	Y	-	P	F	F	Y	S	S	S	I	S	I	S	P	Y	S	G	Y	T	Y
CAT06	S	S	S	S	-	-	L	I	V	Y	S	Y	S	I	S	I	S	S	Y	Y	S	S	T	S
CAT07	Y	Y	S	Y	-	-	L	I	V	S	S	Y	S	I	Y	I	S	S	S	S	G	S	T	Y
CAT08	S	S	S	Y	R	Y	P	L	I	Y	Y	S	S	I	S	I	Y	S	Y	Y	G	Y	T	S
CAT09	Y	V	W	S	S	T	L	I	I	Y	S	S	S	I	S	I	Y	S	Y	Y	G	S	T	Y
generated in 1 mM EGTA																								
TEG31	S	S	S	S	-	-	L	I	F	Y	S	Y	S	I	S	I	Y	S	Y	S	G	S	T	S
TEG32	F	I	Y	W	-	-	P	L	I	S	S	S	S	I	S	I	Y	P	Y	Y	G	Y	T	S
TEG33	S	Y	R	Y	S	-	P	I	F	Y	S	S	S	I	S	I	S	P	Y	Y	S	S	T	S
TEG34	S	S	S	S	-	-	L	I	F	Y	S	Y	S	I	S	I	S	P	Y	Y	S	S	T	S
TEG35	Y	G	G	S	-	-	L	I	I	S	S	S	S	I	S	I	Y	S	S	S	G	S	T	S
TEG36	W	Q	Y	K	-	-	L	I	V	S	S	S	S	I	Y	I	S	P	S	S	G	Y	T	Y
TEG37	Y	F	Y	K	Y	S	L	V	I	S	S	S	S	I	Y	I	S	S	S	Y	G	Y	T	Y

	CDR-H3																				
	94	95	96	97	98	99	100	100a	100b	100c	100d	100e	100f	100g	100h	100i	100j	100k	100l	100m	101
Library	R	X(4-17)																	AG	FILM	D
generated in 1 mM calcium chloride																					
CAT01	R	G	R	K	F	G	S	Y	S	W	F	R	S	Y	-	-	-	-	A	L	D
CAT02	R	K	A	G	Y	Y	F	Y	W	W	Q	L	L	-	-	-	-	-	G	F	D
CAT03	R	P	Y	E	W	Y	W	W	Y	S	G	-	-	-	-	-	-	-	A	F	D
CAT04	R	S	H	Y	W	Y	Y	R	Q	Y	Y	Y	-	-	-	-	-	-	A	L	D
CAT05	R	S	S	Y	Y	Y	Y	Q	P	V	-	-	-	-	-	-	-	-	G	M	D
CAT06	R	S	Y	W	Y	W	R	S	T	L	G	-	-	-	-	-	-	-	G	I	D
CAT07	R	S	Y	Y	L	Y	G	W	W	F	V	W	-	-	-	-	-	-	A	M	D
CAT08	R	W	L	S	Y	E	L	-	-	-	-	-	-	-	-	-	-	-	G	M	D
CAT09	R	W	Q	Y	W	S	G	Y	R	S	P	-	-	-	-	-	-	-	A	M	D
generated in 1 mM EGTA																					
TEG31	R	P	V	Y	Q	P	Y	G	W	W	F	D	R	V	N	R	-	-	G	M	D
TEG32	R	Q	W	F	R	W	W	T	W	Y	Y	Y	-	-	-	-	-	-	A	L	D
TEG33	R	S	S	M	Y	Y	K	Y	F	S	S	S	L	T	G	G	-	-	A	F	D
TEG34	R	S	Y	Y	F	Y	Y	A	T	Q	R	-	-	-	-	-	-	-	G	L	D
TEG35	R	W	Q	L	F	G	Y	Y	F	K	W	Y	W	Q	P	A	Y	-	G	M	D
TEG36	R	Y	R	Q	L	E	F	P	S	Y	A	G	Q	-	-	-	-	-	A	M	D
TEG37	R	Y	Y	E	K	Y	W	Y	S	S	G	-	-	-	-	-	-	-	A	L	D

Fig. S5. Characterization of synthetic Fab fragments generated by phage display. (**a**) Sequences of unique Fabs generated against $AtTPC1_{WT}$ in MSP E3D1 nanodiscs (See Methods). Composition of CDRs (L3, H1, H2, H3) are shown. Enriched YSGW residues are highlighted and numbered according to Kabat. (**b**) Fab-displaying Phage ELISA of $AtTPC1_{WT}$ E3D1 or empty nanodiscs in the presence of 1 mM $CaCl_2$, 1 mM EGTA, 1 μM NAADP, and 1 μM NED19. (**c**) $AtTPC1_{WT}$ ELISA binding of CAT06 in 1 mM $CaCl_2$ or 1 mM EGTA in DDM detergent. (**d**) ELISA Binding of CAT06 to $AtTPC1_{WT}$, $AtTPC1_{DA}$, and $AtTPC1_{DDE}$. (**e**) (top) Size exclusion chromatograph and (bottom) SDS-PAGE gel of $AtTPC1_{DDE}$-CAT06 complex. (**f**) Negative-stain EM analysis of $AtTPC1_{WT}$-CAT06 complex in DDM.

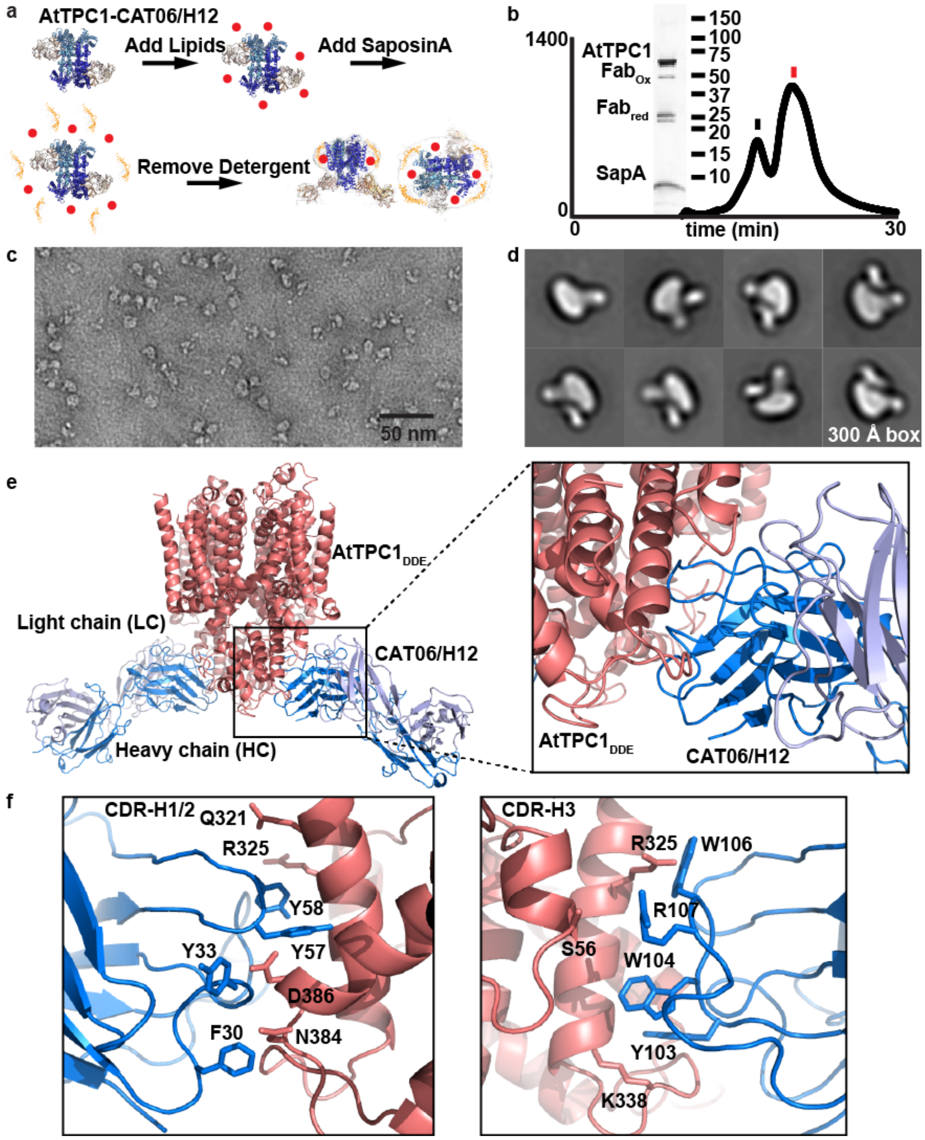

Fig. S6. Reconstitution of AtTPC1$_{DDE}$-CAT06/H12 into saposin A. a, Schematic of the saposin A reconstitution method (See Methods). **b,** Size exclusion chromatograph and SDS-PAGE gel of reconstituted AtTPC1$_{DDE}$-CAT06/H12-saposin A. Labels for oxidized (Fab$_{ox}$) and reduced (Fab$_{red}$) Fab, and saposin A (SapA) are shown. Peak fractions for AtTPC1$_{DDE}$-CAT06/H12-saposin A (black) and saposin A (red) alone are marked. **c, d,** Negative-stain **(c)** micrograph and **(d)** 2D class-averages of AtTPC1$_{DDE}$-CAT06/H12-saposin A. **e,** Overall view of the Fab-bound complex AtTPC1$_{DDE}$-CAT06/H12. VSD2 included in model for clarity. Inset shows interactions between heavy chain (HC) and the EF-hand of AtTPC1$_{DDE}$. **f,** Major residues at the interaction interface between AtTPC1$_{DDE}$ and CAT06/H12: (left) CDR-H1/2, (right) CDR-H3.

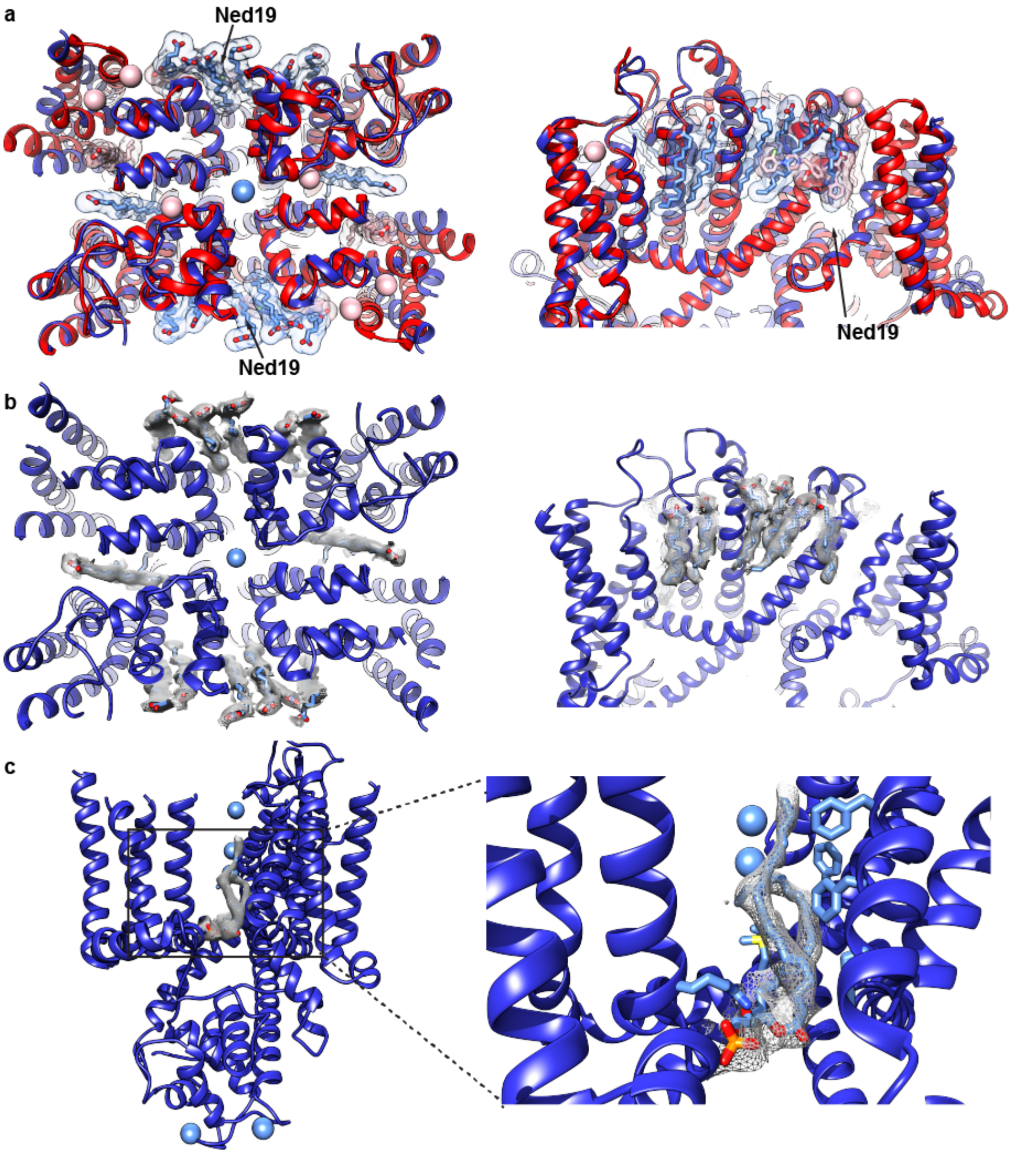

Fig. S7. NED19 and lipid binding sites. a, Overlay of AtTPC1$_{WT}$ crystal structure (red, PDBID 5DQQ) and AtTPC$_{DDE}$ state 1 (blue), highlighting the binding sites for Ned19 and lipid molecules. **b,** Density shown for lipids on the lumenal membrane leaflet. **c,** View of phosphatidic acid binding site on the cytoplasmic membrane leaflet. Inset shows a close up of the molecular interactions. Ca^{2+}-ions shown as spheres.

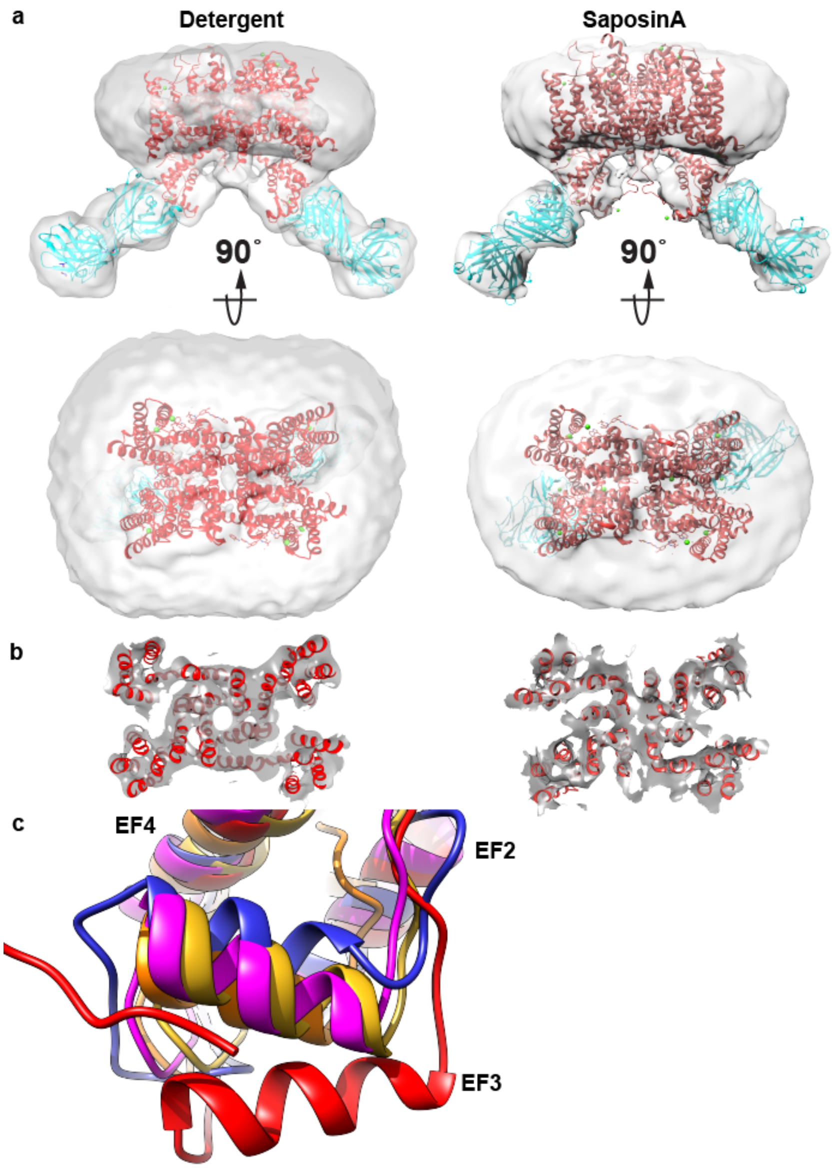

Fig. S8. Comparison on AtTPC1 structures in detergent and saposin. a, Cryo-EM reconstructions of AtTPC1$_{WT}$-4B8 complexes in (left) DDM detergent or (right) reconstituted into saposin A nanoparticles shown at low contour. The gold-standard FSC resolution for the reconstructions are 8Å and 7Å for the detergent and saposin A samples, respectively. **b,** Sections through cryo-EM reconstructions shown in **(a)** at higher contour to emphasize the visibility of transmembrane helices. **c,** Overlay of refined AtTPC1$_{DDE}$-CAT06/H12-saposin A cryo-EM structure (blue), and rosetta-fit models of AtTPC1$_{WT}$-CAT06/H12-saposin A (pink), AtTPC1$_{WT}$-4B8-saposin A (gold), and (orange) AtTPC1$_{WT}$-4B8 in DDM detergent in the presence of 1mM tetrandine and 1mM Ned19 (gold), and the AtTPC1$_{WT}$ crystal structure (red, PDBID 5DQQ).

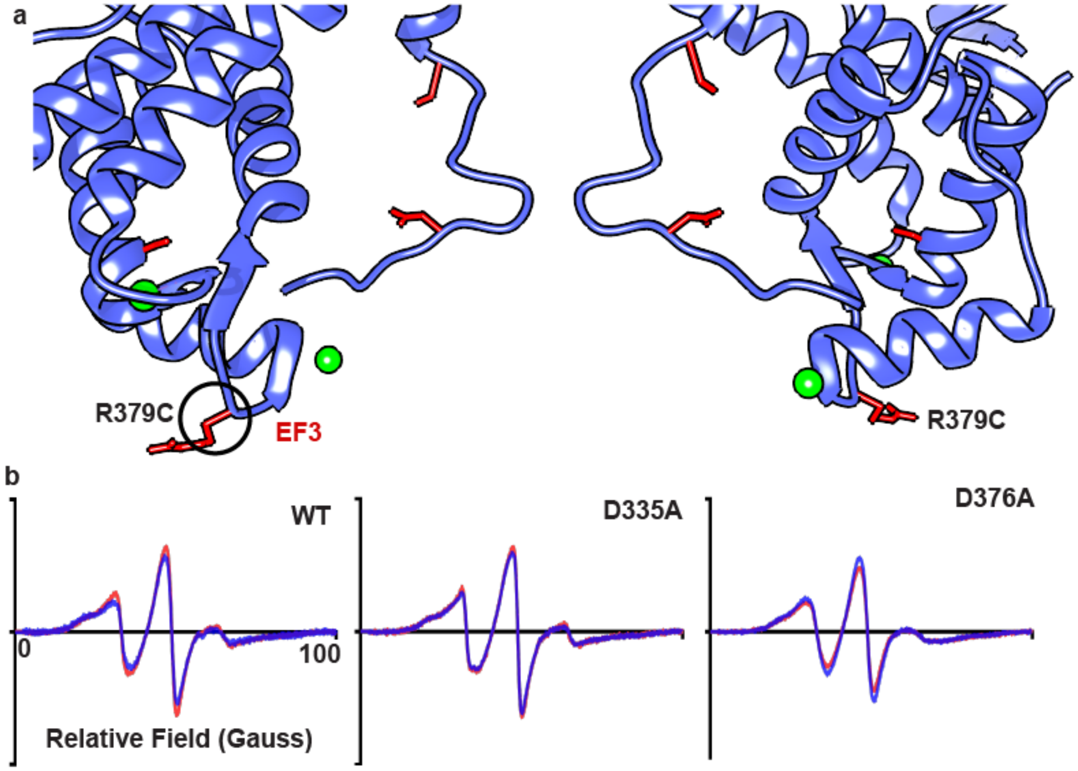

Fig. S9. EPR Spectroscopy of EF-hand. a, Locations of spin probe labeling in the EF-domain, CTD, and Gate analyzed by CW-EPR spectroscopy are shown in red overlaid onto the structure of AtTPC1 (PDBID 5DQQ). **b,** CW-EPR spectra of MTSL-labeled AtTPC1$_{\text{cysless}}$ R379C in (left) wild-type, (middle) D335A, and (right) D376A background, collected in the presence of Ca^{2+} (blue) or EGTA (red). Y-axis is in arbitrary units.

Data collection[a]				
Voltage (kV)	300			
Pixel size (Å)	1.2156			
Defocus range (µm)	-0.8 – -2.0			
Total electron dose (e^-/A^2)	60			
Exposure time (s)	12			
Number of frames/image	60			
Number of images	3,408			
Image processing[a,b]				
Map	**High-res**	**State 1**	**State 2**	**Fab-bound**
Autopicked particles	996,035			
Particles post 2D	409,531			
Final particle number	224,577	44,353	67,308	224,577
Resolution (unmasked, Å)	3.7	4.2	4.3	4.0
Resolution (masked, Å)	3.3	3.7	3.7	3.7
Sharpening B-factor (Å^2)	-117	-95	-86	-104
Refinement[a,c]				
Number of atoms	8913	10682	10697	11641
R.m.s. deviations				
Bond lengths (Å)	0.017	0.014	0.009	0.018
Bond angles (°)	1.481	1.305	1.090	1.679
Ramachandran				
Favored (%)	91.49	91.59	92.95	88.32
Allowed (%)	8.41	8.25	6.89	11.39
Outlier (%)	0.10	0.16	0.16	0.29
Mean B-factor (Å^2)[d]	101.80	142.71	201.66	100.50
Molprobity Clashscore[e]	5.51	7.96	7.47	8.36
EMRinger score[f]	3.94	1.63	1.42	2.92
PDB ID[g]	6E1M	6E1N	6E1P	6E1K
EMDB ID[g]	8957	8958	8960	8956

[a] Data collection and processing detailed in Methods.

[b] Image processing schematic in Extended Data Fig. 4.

[c] Real-space refinement in PHENIX as outlined in Methods.

[d] As implemented in PHENIX, number of clashes per 1000 atoms.

[e] Calculated from real-space refinement in PHENIX.

[f] Calculated using EMRinger in PHENIX.

[g] Deposition codes for coordinates and maps deposited to the Protein Data Bank and Electron Microscopy Data Bank.

Table S1. Cryo-EM data collection and refinement statistics.

Data Collection	**AtTPC1$_{\mathbf{DA}}$**[a]
Beamline	ALS 8.3.1 ALS 5.0.2 SSRL 12-2
Space Group	$C222_1$
Cell Dimensions	a=88.47, b=154.42, c=218.45, $\alpha=\beta=\gamma=90$
Wavelength (Å)	1.000
Resolution[b]	30-3.5(4-3.5)
Number of reflections	19231
Completeness (%)	99.7(99.8)
Multiplicity	13.3(13.6)
I/σI	8(0.93)
$CC_{1/2}$[c]	100(57.7)
Rmeas (%)	23.6(362.2)
Anisotropy (a, b, c)[d]	3.5 x 6.0 x 4.5Å
Refinement	
Resolution (Å)	3.5 x 6.0 x 4.5Å[e]
No. reflections	8954
$R_{\text{work}}/R_{\text{free}}$	0.3184/0.3519[f]
No. atoms	5092
Protein	5054
Ligand/ion	38
B-factor	114.26
R.M.S. deviations	
Bond lengths (Å)	0.003
Bond angles (º)	0.687
Ramachandran (%)	
Favored	93.09
Allowed	6.25
Outliers	0.66
PDB ID[g]	6CX0

[a] Uncorrected native data

[b] Values in parenthesis are for highest resolution shell.

[c] Percentage of correlation between intensities from random half-datasets, as calculated in XDS.

[d] Anisotropy as determined by Diffraction Anisotropy Server.

[e] Anisotropy-corrected data used for refinement with sharpening B-factor of -142.05 Å^2.

[f] 5% of reflections were omitted from refinement for the calculation of R_{free}.

[g] Deposition codes for coordinates and maps deposited to the Protein Data Bank and Electron Microscopy Data Bank.

Table S2. X-ray Data Collection and Refinement Statistics for AtTPC1$_{\mathbf{DA}}$

Movie S1. Morph between resting-state AtTPC1$_{WT}$ and intermediate activated states of AtTPC1$_{DDE}$ in state 1 and 2. AtTPC1$_{WT}$ (red) and intermediate activated states of AtTPC1$_{DDE}$ in state 1 (blue) and 2 (pink) are shown overlaid sequentially, then colored by individual domain for the morph trajectory.

References

1. Tribet C, Audebert R, Popot J-L (1996) Amphipols: Polymers that keep membrane proteins soluble in aqueous solutions. *Proc Natl Acad Sci U S A* 93(26):15047–15050.

2. Ritchie TK, et al. (2009) Chapter Eleven - Reconstitution of Membrane Proteins in Phospholipid Bilayer Nanodiscs. *Methods in Enzymology*, Liposomes, Part F., ed Düzgünes N (Academic Press), pp 211–231.

3. Frauenfeld J, et al. (2016) A saposin-lipoprotein nanoparticle system for membrane proteins. *Nat Methods* 13(4):345–351.

4. Wu S, et al. (2012) Fabs enable single particle cryoEM studies of small proteins. *Struct Lond Engl 1993* 20(4):582–592.

5. Pardon E, et al. (2014) A general protocol for the generation of Nanobodies for structural biology. *Nat Protoc* 9(3):674–693.

6. Galfre G, Howe SC, Milstein C, Butcher GW, Howard JC (1977) Antibodies to major histocompatibility antigens produced by hybrid cell lines. *Nature* 266(5602):550–552.

7. Dominik PK, et al. (2016) Conformational Chaperones for Structural Studies of Membrane Proteins Using Antibody Phage Display with Nanodiscs. *Structure* 24(2):300–309.

8. Bethke PC, Jones RL (1997) Reversible protein phosphorylation regulates the activity of the slow-vacuolar ion channel. *Plant J* 11(6):1227–1235.

9. Cang C, et al. (2013) mTOR Regulates Lysosomal ATP-Sensitive Two-Pore Na+ Channels to Adapt to Metabolic State. *Cell* 152(4):778–790.

10. Kintzer AF, Stroud RM (2016) Structure, inhibition and regulation of two-pore channel TPC1 from Arabidopsis thaliana. *Nature* 531(7593):258–264.

11. Kintzer AF, Stroud RM (2018) On the structure and mechanism of two-pore channels. *FEBS J* 285(2):233–243.